# Hydrogen Production and Degradation of Ciprofloxacin by Ag@TiO$_2$-MoS$_2$ Photocatalysts

Abniel Machín [1,*], Kenneth Fontánez [2], Diego García [3], Paola Sampayo [3], Carla Colón-Cruz [3], Gerardo J. Claudio-Serrano [3], Loraine Soto-Vázquez [4], Edgard Resto [4], Florian I. Petrescu [5], Carmen Morant [6] and Francisco Márquez [3,*]

[1] Arecibo Observatory, Cupey Campus, Universidad Ana G. Méndez, San Juan, PR 00926, USA
[2] Department of Chemistry, Río Piedras Campus, University of Puerto Rico, San Juan, PR 00925, USA; kenneth.fontanez@upr.edu
[3] Nanomaterials Research Group, Division of Natural Sciences and Technology, Gurabo Campus, Universidad Ana G. Méndez, Gurabo, PR 00778, USA; diego.garcia13@upr.edu (D.G.); psierra5@email.uagm.edu (P.S.); ccolon265@email.uagm.edu (C.C.-C.); gclaudio17@email.uagm.edu (G.J.C.-S.)
[4] Materials Characterization Center Inc., Molecular Sciences Research Center, University of Puerto Rico, San Juan, PR 00926, USA; sotol6@uagm.edu (L.S.-V.); edgar.resto@upr.edu (E.R.)
[5] International Federation for the Promotion of Mechanism and Machine Science (IFToMM), Romanian Association for Theory of Machines and Mechanisms (ARoTMM), Bucharest Polytechnic University, 060042 Bucharest, Romania; florian.petrescu@upb.ro
[6] Department of Applied Physics, Instituto de Ciencias de Materiales Nicolás Cabrera, Autonomous University of Madrid, 28041 Madrid, Spain; c.morant@uam.es
* Correspondence: machina1@uagm.edu (A.M.); fmarquez@uagm.edu (F.M.); Tel.: +1-787-878-2612 (ext. 220) (A.M.); +1-787-743-7979 (ext. 4250) (F.M.)

Abstract: The photocatalytic activity of silver-based catalysts containing different amounts of molybdenum disulfide (MoS$_2$; 5, 10 and 20 wt.%) was evaluated by the degradation of the antibiotic ciprofloxacin and the production of hydrogen via water splitting. All the silver (Ag)-based catalysts degraded more than 70% of the antibiotic in 60 min. The catalyst that exhibited the best result was 5%Ag@TiO$_2$-P25-5%MoS$_2$, with ca. 91% of degradation. The control experiments and stability tests showed that photocatalysis was the degradation pathway and the selected silver-based catalysts were stable after seven cycles, with less than 2% loss of efficiency per cycle and less than 7% after seven cycles. The catalyst with the highest hydrogen production was 5%Ag@TiO$_2$ NWs-20%MoS$_2$, 1792 μmol/hg, at a wavelength of 400 nm. This amount was ca. 32 times greater than that obtained by the pristine titanium oxide nanowires catalyst. The enhancement was attributed to the high surface area of the catalysts, along with the synergism created by the silver nanoparticles and MoS$_2$. All the catalysts were characterized by X-ray photoelectron spectroscopy (XPS), X-ray diffraction (XRD), Raman spectroscopy, field-emission scanning electron microscopy (FE-SEM), high-resolution transmission electron microscopy (HRTEM), Brunauer–Emmett–Teller (BET) surface area analysis and energy dispersive X-ray spectroscopy (EDS).

Keywords: photocatalysis; Ag NPs; MoS$_2$; ciprofloxacin; hydrogen production

1. Introduction

Industrial development, together with energy shortages and overpopulation of the planet, is perhaps among the most relevant factors affecting the environment and the future sustainable development of society [1–7]. Serious environmental pollution problems, which are ultimately responsible for global warming, are becoming increasingly important [3]. However, despite the fact that the current situation of the planet was already predicted a few decades ago, we are very far from any reversal of the problems generated by economic and social development.

Chemical catalysis was a pioneer in addressing the development of new eco-friendly alternatives to solve the shortage of energy resources and, at the same time, enable the development of advanced methods to fight environmental pollution [1,8,9]. In this regard, chemical compounds that emulate the same mechanism as nature can be a realistic alternative that allows for solving a large part of these problems [9]. Hydrogen production by electrochemical water splitting is considered a simple and sustainable method of obtaining clean hydrogen, as energy carrier, through a hydrogen evolution reaction (HER) [4,5,10–13]. Until now, the most effective materials for catalyzing HER have been the metals of the platinum (Pt) group [5,12,14]. Current research is based on developing new high-performance and cost-effective catalysts that can be easily synthesized and that reduce enormous production costs (e.g., nanoparticles and nanocrystals, transition metal chalcogenides, metal carbides or hydroxides, among others) [1,5,15].

To date, titanium oxide (TiO_2) has been one of the most widely used photocatalysts, due to its stability, resistance to corrosion, availability in nature and low cost [7,16]. However, the great limitation of TiO_2 is due to its wide bandgap, which makes its practical use difficult [7,16]. As a solution to this problem, TiO_2 can be synthesized in different crystalline structures and forms and modified by adding noble metals to reduce the band gap and optimize the use of sunlight [7]. The incorporation of silver (Ag) nanoparticles on the surface of TiO_2 makes it possible to change the properties of the semiconductor and diminish the rapid recombination of the photogenerated charge carriers in the process, shifting the radiation absorption threshold to the visible region [17]. The reason for this behavior is the surface plasmon resonance effect and charge separation by the displacement of photoexcited electrons from the metal nanoparticles to the conduction band (CB) of TiO_2 [17]. Molybdenum disulfide (MoS_2) is considered a promising HER catalyst due to its high catalytic activity, high abundance, and low cost [6,12,18]. There are different experimental procedures that allow for synthesizing MoS_2 in a simple way, although its use is certainly limited by the intrinsic semiconductor behavior and the number of active sites [4,6,19]. To improve this behavior, and in the same way that has been addressed with TiO_2, different strategies have been developed to modify morphology, specific surface and even the presence of structural defects induced by metal doping (e.g., Pt, Cr, Mn, V) [1,7,11].

In the case of TiO_2, morphology and crystallographic structure are determining factors to regulate its applicability to different processes [7,16]. TiO_2 nanowires (TiO_2NWs), with a rutile-type crystalline structure, have shown high catalytic activity, which could later be improved by doping with appropriate metals [1,7,8,16]. In the case of two-dimensional materials such as MoS_2, the different synthesis procedures produce crystals formed by the adhesion of a large number of layers [20]. Opening these 2D materials is an effective way to alter the physical and chemical properties, such as the conductivity or band gap and, of course, its catalytic activity [3,20].

In the present research we synthesized different catalysts based on silver nanoparticles on TiO_2NWs with a rutile structure, to which MoS_2 (5, 10, 20 wt.%) was added. These rutile nanowire-based catalysts were also compared with other catalysts synthesized from commercial TiO_2 (TiO_2-P25). The main objective has been to combine some of the materials that have shown adequate catalytic behavior in order to obtain adducts with improved properties. To the best of our knowledge, the hybrid materials prepared in this research are novel and, as is described later, they can be used efficiently in catalytic environmental decontamination processes and in photocatalytic hydrogen production by water splitting.

2. Results and Discussion

2.1. Characterization of the Catalysts

The morphology of the as-synthesized titanium oxide nanowire (TiO_2NW) and its commercial form (TiO_2-P25) was studied by field-emission scanning electron microscopy (FE-SEM), and the results are shown in Figure 1. As it can be seen, the TiO_2NWs (Figure 1a,b) consisted of nanowires with different lengths and diameters. At a higher magnification (Figure 1c) it can be noticed that the nanowires have a square-like form with different

domains and sizes. A BET analysis (see Table 1) found that the nanowires had a high surface of 403 m^2g^{-1}, which can be explained by the highly branched structures of the wires. This high surface area could increase the catalytic properties of the composite. Figure 1d shows the FE-SEM micrograph of the titanium oxide commercial form (TiO_2-P25), and, as can be seen there, this catalyst consists of aggregates of irregular sphere-like particles with diameters ranging from ca. 50 to 75 nm.
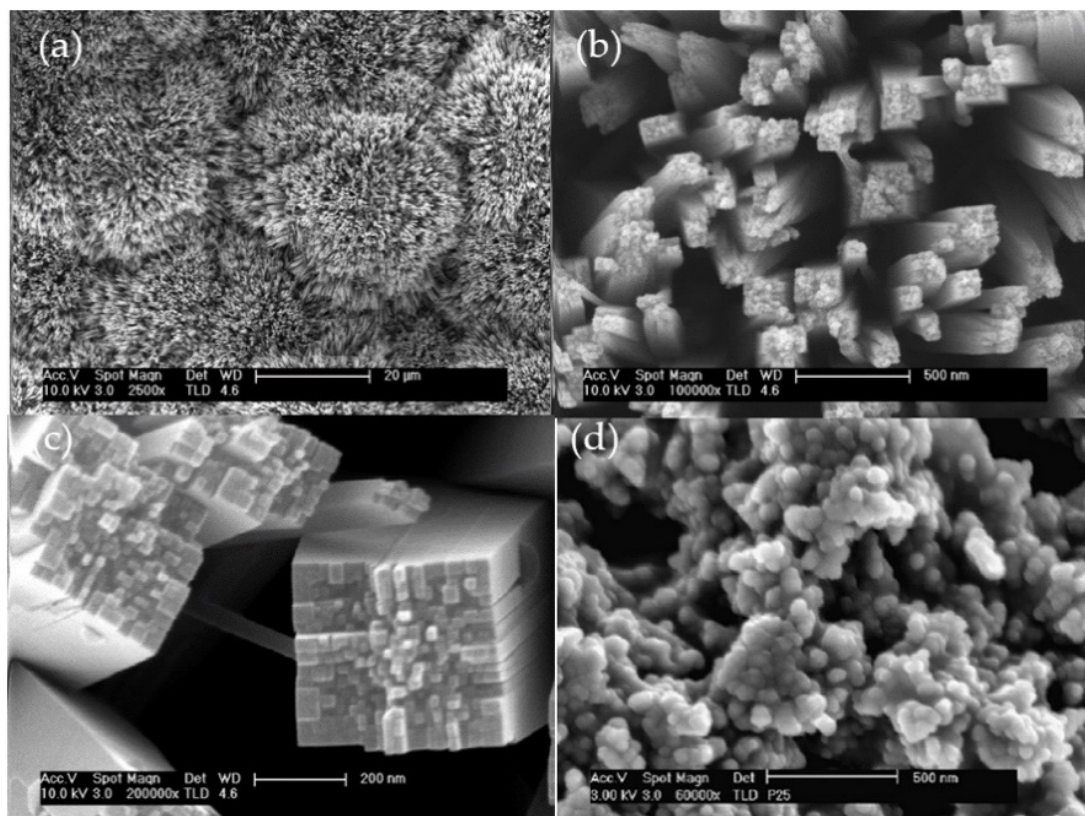

Figure 1. FE-SEM micrographs of TiO_2NW (**a**–**c**) and its commercial form (TiO_2-P25) (**d**), at different magnifications.

Table 1. Brunauer, Emmett and Teller (BET) surface area of catalysts containing silver and MoS_2 *.

Catalyst	TiO_2-P25 (m^2g^{-1})	TiO_2NWs (m^2g^{-1})
0% (Unmodified)	53	403
5% MoS_2	98	429
10% MoS_2	129	443
20% MoS_2	172	491

* All the catalysts have a silver loading of 5 wt.%.

Figure 2 shows the FE-SEM and energy dispersive X-ray spectroscopy (EDS) of the 5%Ag@TiO_2NWs-5%MoS_2 catalyst. As can be seen in Figure 2a,b, the TiO_2NWs varies in length and width, which is attributed to the catalyst synthesis parameters, and the incorporation of silver nanoparticles (AgNPs) and molybdenum disulfide (MoS_2). The incorporation of AgNPs and MoS_2 onto the TiO_2NWs was non-homogenous, and the particles presented different sizes and shapes. The EDS mapping of the catalyst showed the presence of titanium (Figure 2c; green), silver (Figure 2d; blue), molybdenum (Figure 2e; orange), and sulfur (Figure 2f; red) with sufficient dispersion, although some aggregates of MoS_2 were observed. The rest of the catalysts (not shown) presented a similar trend.
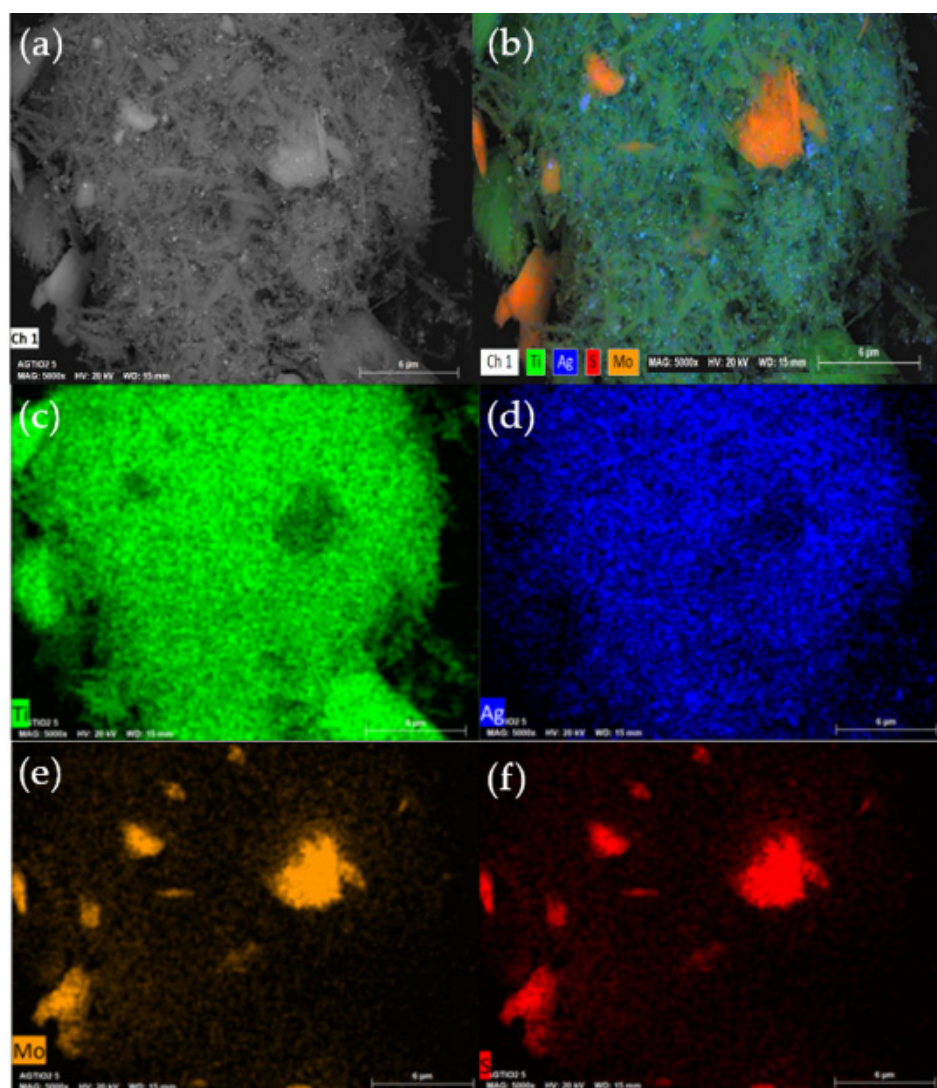
Figure 2. FE-SEM (**a**) and EDS images (**b–f**) of the 5Ag%TiO$_2$NWs-5%MoS$_2$ catalyst.

Figure 3 shows the high-resolution transmission electron microscopy (HRTEM) micrographs of 5%Ag@TiO$_2$NWs-5%MoS$_2$ and 5%Ag@TiO$_2$-P25-5%MoS$_2$. As can be seen, the distribution of titanium oxide (TiO$_2$; yellow arrows), silver nanoparticles (AgNPs; white arrows) and MoS$_2$ (red arrows) is quite homogeneous. A spacing may be observed in Figure 3c of ca. 0.290 nm for the TiO$_2$ NWs, which corresponds to the (110) plane of the rutile crystalline phase of the nanowires, and a spacing of ca. 0.234 nm between adjacent lattice planes in the AgNPs, with particle diameters of less than 10 nm. Huerta-Aguilar and group [21] assigned the spacing measured to the (111) plane of the Ag lattice. Previous works [16,22–25] reported similar results when sodium borohydride (NaBH$_4$) was used as a reducing agent. The MoS$_2$ (see Figure 3d) presented a spacing of ca. 0.274 nm and has been attributed to the (100) plane [18].

Table 1 shows the BET surface area of the composites containing silver and MoS$_2$ (5, 10 and 20 wt.%). As can be seen, the surface area of the unmodified catalysts (53 m^{2}g^{-1} for TiO$_2$-P25, and 403 m^{2}g^{-1} for TiO$_2$ NWs) increased with the incorporation of silver and MoS$_2$. The highest surface area was reported to be 491 m^{2}g^{-1} and was obtained with the 5%Ag@TiO$_2$ NWs-20%MoS$_2$ catalyst. For the commercial catalyst, the highest surface area (172 m^{2}g^{-1}) was also obtained with the catalysts containing a MoS$_2$ loading of 20 wt.% (5%Ag@TiO$_2$-P25-20%MoS$_2$). Previous works [16,22–25] have shown a direct relationship between the surface area and the amount of hydrogen produced.
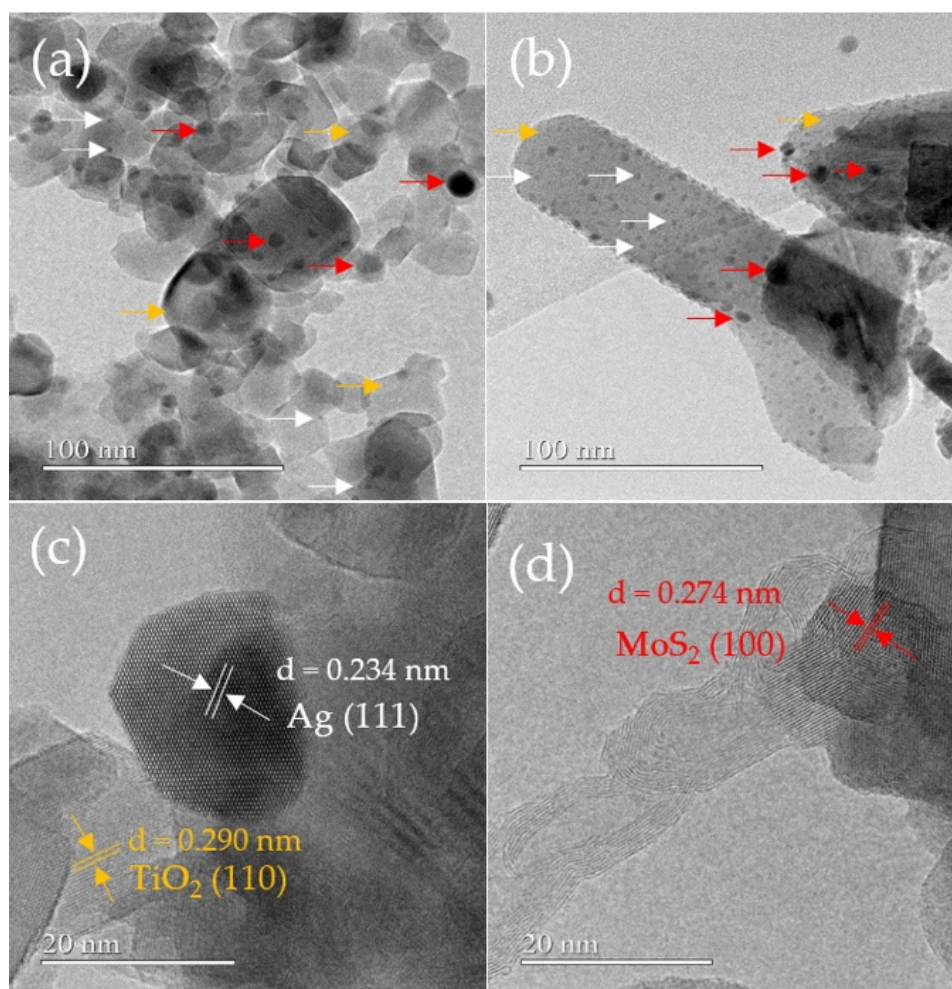
Figure 3. High-resolution transmission electron microscopy (HRTEM) micrographs of 5Ag%TiO$_2$-P25-5%MoS$_2$ (**a**), and 5Ag%TiO$_2$NWs-5%MoS$_2$ (**b**). (**c**) shows a magnification of AgNPs with a lattice spacing of ca. 0.234 nm, and the lattice spacing of the TiO$_2$ NWs. (**d**) presents the spacing lattice of MoS$_2$. The white, red, and yellow arrows show the AgNPs, MoS$_2$, and TiO$_2$, respectively.

The catalysts were also characterized by X-ray photoelectron spectroscopy (XPS). Figure 4 shows the most relevant transitions considering the catalyst with the highest MoS$_2$ load (5%Ag@TiO$_2$NWs-20%MoS$_2$). Figure 4a shows the transition corresponding to Ti2p. As can be seen, two components are shown that were ascribed to the Ti2p$_{3/2}$ and Ti2p$_{1/2}$ transitions. Each transition was deconvolved to two peaks. In the case of Ti2p$_{3/2}$, the most intense peak is shown at 458.3 eV, and it was unambiguously assigned to Ti^{4+} in TiO$_2$ [24,26,27]. Additionally, another less intense peak is shown at 458.9 eV that was assigned to the Ti species with oxygen vacancies, which suggests the presence of Ti^{3+} [26,27]. The same behavior observed in the Ti2p$_{3/2}$ transition is observed in Ti2p$_{1/2}$, with a 5.8 eV spin-orbit splitting. Figure 4b shows the transition corresponding to O1s. As can be seen, the transition is clearly asymmetric and was deconvolved to two components at ca. 529.8 and 531 eV. The most intense peak was assigned to oxygen in the TiO$_2$ network, while the component observed at 531 eV was assigned to oxygen vacancies in the TiO$_2$ network or to non-lattice oxygen [28,29]. These results are in agreement with those obtained for Ti2p. Figure 4c represents the transition of Ag3d, with peaks at 374 and 368.1 eV, and a characteristic spin-orbit splitting of ca. 6.0 eV, which were clearly assigned to the presence of metallic Ag [26,27]. The Mo3d core level peak region of the MoS$_2$ is shown in Figure 4d. The Mo3d shows two peaks at 228.9 and 232 eV, which were attributed to the doublet Mo3d$_{5/2}$ and Mo3d$_{3/2}$, respectively, characteristic of the Mo^{4+} state in MoS$_2$ [30]. The

shoulder observed at 226.4 eV was assigned to S2s, typical of MoS_2. The width and symmetry of the peaks is consistent with the absence of additional oxidation states for Mo. The region corresponding to S2p is shown in Figure 4e. As can be seen, the peak shows a clear asymmetry that has allowed it to be decomposed into the two typical components of spin-orbit splitting at 161.6 eV and 162.9 eV ($S2p_{3/2}$ and $S2p_{1/2}$, respectively), characteristic of S^{2-} in MoS_2 [31].
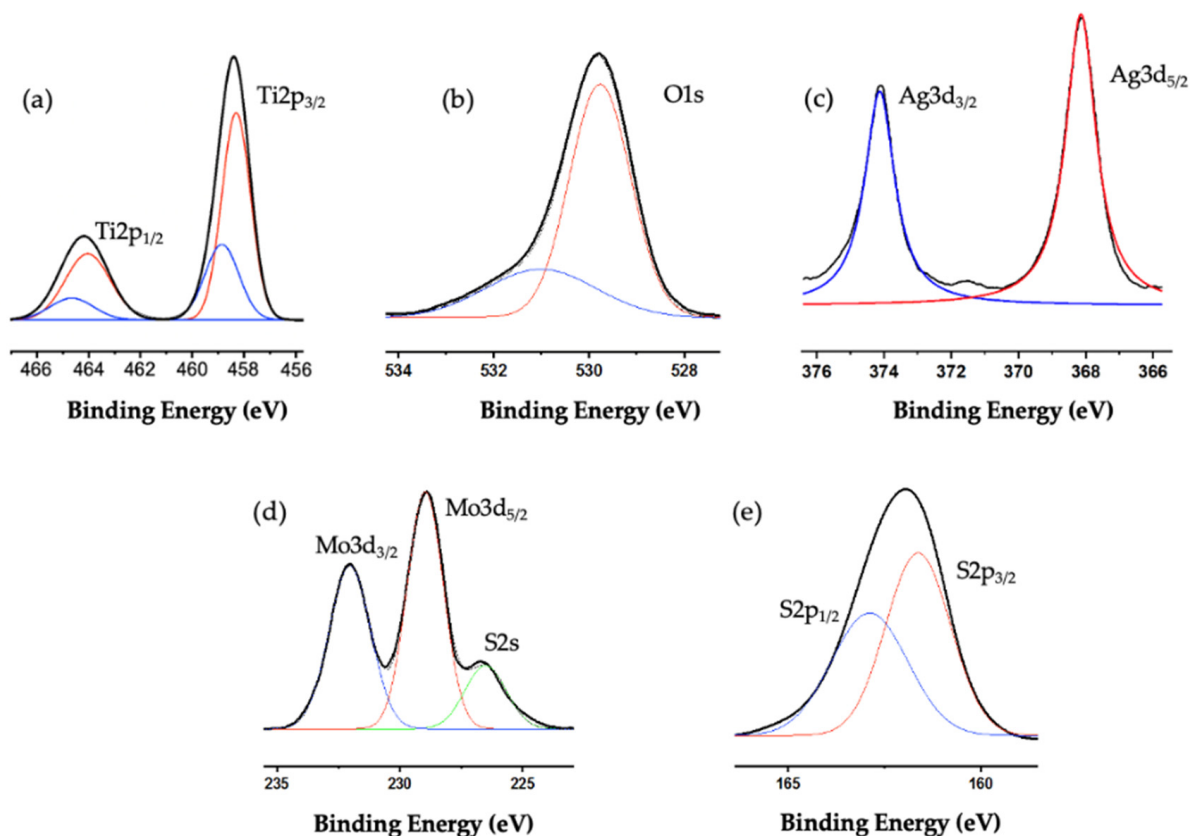

Figure 4. XPS spectra of Ti 2p (**a**), O 1s (**b**), Ag3d (**c**), Mo3d (**d**), and S2p (**e**) from 5%Ag@TiO$_2$ NW-20%MoS$_2$.

The X-ray diffraction patterns of the silver-based catalysts with different MoS_2 loadings are shown in Figure 5. 5%Ag@TiO$_2$-P25-X%MoS$_2$ (Figure 5a), shows intense peaks at 25° (101), 38° (004), 48° (220), 54° (105) and 55° (211), which were assigned to the crystalline phase of TiO_2 anatase [24,32]. Additionally, other peaks were observed at 27° (110), 36° (101), 41° (111) and 54° (211), assigned to the rutile TiO_2 crystalline phase [24,32]. The MoS_2 characteristic peaks can be seen at 33° (100), 39° (103), 50° (105) and 57° (110) [33–35]. In the case of AgNPs, a small but distinguishable peak was observed at 46° (200) [24,32]. The peak associated with silver (111) was not detected due to the overlap with a characteristic peak of anatase at the same angle (38°). The diffraction patterns corresponding to the 5%Ag@TiO$_2$NWs-X%MoS$_2$ composites are shown in Figure 5b. The peaks observed at 27°, 36° and 55° were assigned to the (110), (101) and (211) planes, respectively, of the rutile crystalline phase of TiO_2. The most characteristic peaks of MoS_2 were also observed at 33° (100), 39° (103) and 60° (110) [33–35]. The presence of AgNPs was evidenced by two peaks at 38° and 46°, corresponding to the crystallographic planes (111) and (200), respectively [24,32].
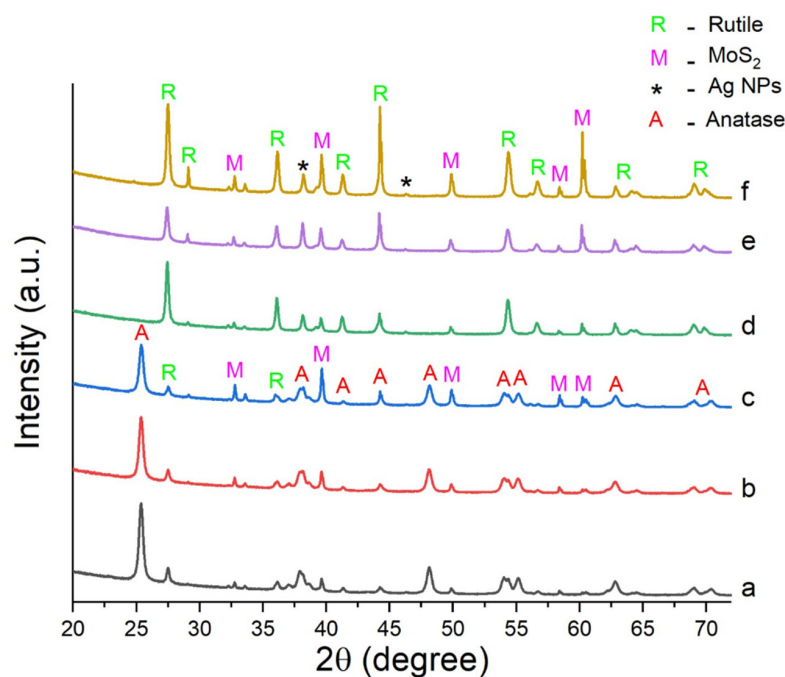
Figure 5. X-ray diffraction patterns (XRD) of 5%Ag@TiO$_2$-P25-5%MoS$_2$ (**a**), 5%Ag@TiO$_2$-P25-10%MoS$_2$ (**b**), 5%Ag@TiO$_2$-P25-20%MoS$_2$ (**c**), 5%Ag@TiO$_2$NWs-5%MoS$_2$ (**d**), 5%Ag@TiO$_2$ NWs-10%MoS$_2$ (**e**), 5%Ag@TiO$_2$NWs-20%MoS$_2$ (**f**).

The Raman spectroscopy results of the silver-based catalysts can be seen in Figure 6. 5%Ag@TiO$_2$-P25-X%MoS$_2$ shows the typical bands of the anatase phase at 150, 395, 510 and 630 cm^{-1}, corresponding to the active vibrational modes of E$_{g(1)}$, B$_{1g(1)}$, A$_{1g}$ + B$_{1g(2)}$, and E$_{g(2)}$, respectively [24,36]. MoS$_2$ has characteristics bands at 383 and 408 cm^{-1} [34] that were not visible due to overlap with the TiO$_2$-P25 bands at 395 and 410 cm^{-1}. In the case of AgNPs, no bands were detected, mainly due to their small diameters (less than 10 nm) and the low concentrations of silver in the composites [37–39]. 5%Ag@TiO$_2$ NWs-X%MoS$_2$ (Figure 6b) showed characteristics bands at 254, 410 and 607 cm^{-1}, corresponding to the B$_{1g}$, E$_g$ and A$_{1g}$ vibrational modes of the rutile crystalline phase of TiO$_2$ [24,37]. As mentioned before, the MoS$_2$ bands at 383 and 408 cm^{-1} were also not detected due to overlap with bands of TiO$_2$NWs. As seen with the TiO$_2$-P25 catalysts, no bands due to silver were observed.

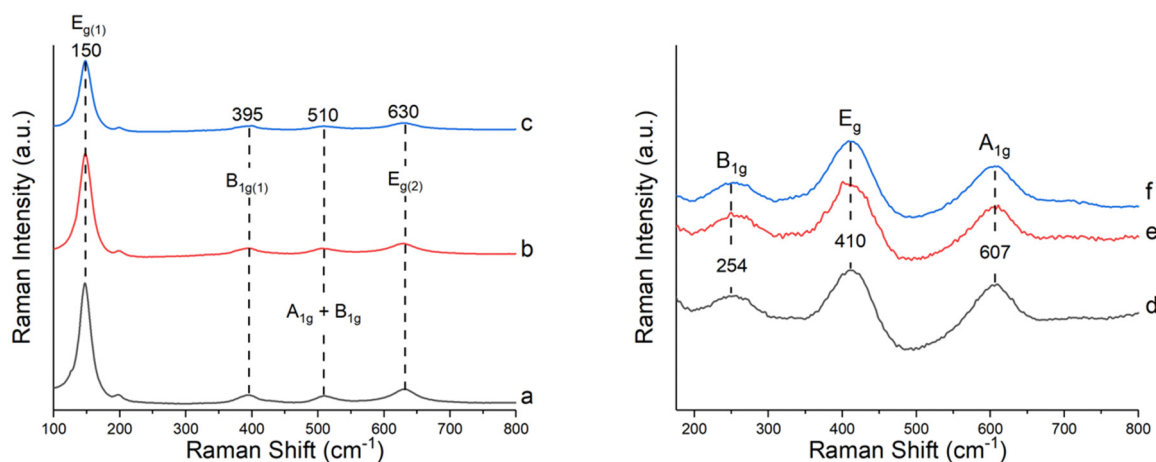**Figure 6.** Raman spectra of 5%Ag@TiO$_2$-P25-5%MoS$_2$ (**a**), 5%Ag@TiO$_2$-P25-10%MoS$_2$ (**b**), 5%Ag@TiO$_2$-P25-20%MoS$_2$ (**c**), 5%Ag@TiO$_2$NWs-5%MoS$_2$ (**d**), 5%Ag@TiO$_2$NWs-10%MoS$_2$ (**e**), and 5%Ag@TiO$_2$NWs-20%MoS$_2$ (**f**).

2.2. Photodegradation of Ciprofloxacin

The degradation efficiency of the photocatalysts was studied based on 60 min timeframe experiments, and considering sample aliquots every 10 min (see Figure 7). The different combinations employed (pristine TiO_2NWs, 5%Ag@TiO_2NWs and 5%Ag@TiO_2NWs-X%MoS_2) showed a continuous degradation through the time (Figure 7a) with no noticeable saturation effect. Moreover, from the five combinations or treatments employed, the three most active catalysts were obtained when MoS_2 was incorporated. These results are in agreement with those from previous studies that demonstrated the improvement of the photocatalytic activity of TiO_2 when MoS_2 is incorporated [40]. The pristine nanowires showed the lower degradation with ca. 70% while the most efficiency combination was 5%AgTiO_2NWs-5%MoS_2. At higher MoS_2 loadings, the degradation decreases, which can be attributed to a saturation of the nanoparticles in the aqueous media causing a light scattering of the radiation (see Table 2). Similar results are observed when TiO_2-P25 is employed as the TiO_2 source. As shown in Figure 7b, all the TiO_2-P25 combinations produced degradation rates of at least 82%. This process has been proved to be cost-effective since it was demonstrated to degrade a persistent organic pollutant at a higher rate in less time compared to similar research [41,42]. When the TiO_2NWs and TiO_2-P25 combinations are compared, it is observed that TiO_2-P25 composites showed better photocatalytic activity despite the fact that TiO_2NWs showed a higher surface area. This might be due to the fact that TiO_2-P25 is primarily composed of anatase phase (+70%), which traditionally has been recognized to be favorable for photocatalytic activity due to a lower recombination rate [43]. To investigate the kinetic behavior of ciprofloxacin photodegradation, pseudo-first-order kinetics was studied by plotting $-\ln(C/Co)$ against irradiation time. The results obtained are shown in Table 3, indicating that the apparent rate constant of the catalysts depends on the percentage of MoS_2 on the catalyst surface.
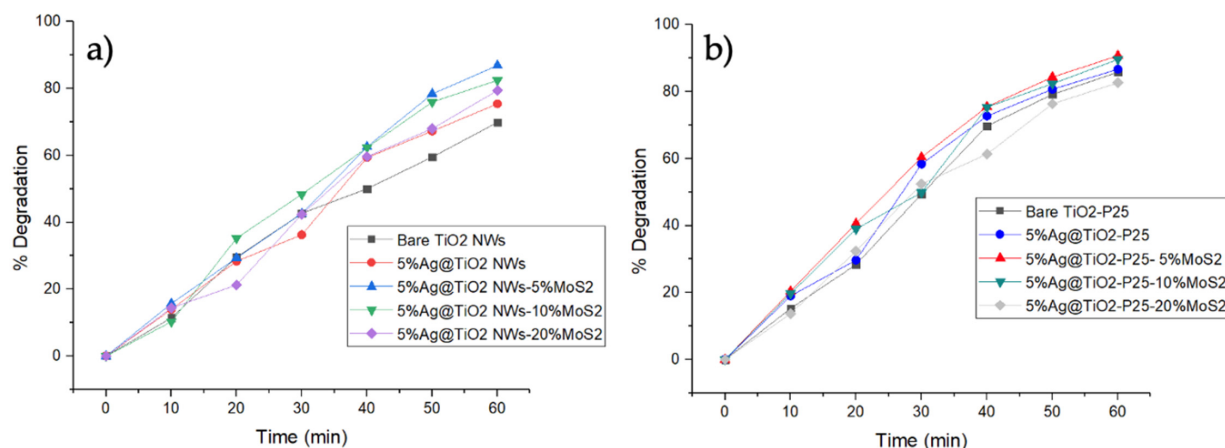
Figure 7. Ciprofloxacin degradation rate (expressed as percent degradation), by using 5%Ag@TiO_2NWs-X%MoS_2 (**a**) and 5%Ag@TiO_2-P25-X%MoS_2 (**b**) catalysts. Estimated error is ca. 5%.

Table 2. Degradation percentages of ciprofloxacin using silver-based catalysts with different MoS_2 loadings.

Catalyst	Ag Loading (wt.%)	MoS_2 Loading (wt.%)	Degradation (%) *
TiO_2-P25	5	0	87
		5	91
		10	90
		20	83
TiO_2NWs	5	0	75
		5	87
		10	82
		20	79

Table 2. *Cont.*

Catalyst	Ag Loading (wt.%)	MoS$_2$ Loading (wt.%)	Degradation (%) *
TiO$_2$-P25 (pristine)	-	-	86
TiO$_2$NWs (pristine)	-	-	70

* Estimated error is ca. 5%.

Table 3. The pseudo-first-order kinetics constants for the photodegradation of ciprofloxacin using TiO$_2$NW- and TiO$_2$-P25-based catalysts.

Catalyst	Apparent Rate [1]	R^2
TiO$_2$NWs	0.019	0.99
5%Ag@TiO$_2$NWs	0.022	0.98
5%Ag@TiO$_2$NWs-5%MoS$_2$	0.029	0.96
5%Ag@TiO$_2$NWs-10%MoS$_2$	0.027	0.99
5%Ag@TiO$_2$NWs-20%MoS$_2$	0.023	0.98
TiO$_2$-P25	0.030	0.98
5%Ag@TiO$_2$-P25	0.032	0.99
5%Ag@TiO$_2$-P25-5%MoS$_2$	0.036	0.99
5%Ag@TiO$_2$-P25-10%MoS$_2$	0.034	0.98
5%Ag@TiO$_2$-P25-20%MoS$_2$	0.027	0.99

[1] (k, min^{-1}).

2.3. Stability Tests

The relevance of these photocatalysts is that ciprofloxacin, as a persistent organic compound, does not degrade under normal conditions, as shown in Figure 8a,b. For both types of catalysts (TiO$_2$-P25 and TiO$_2$ NWs), it is shown that the main degradation pathway is the photocatalysis. The contribution of the photolysis or catalysis pathway (without catalyst or without irradiation, respectively) represents less than 7% in any case.
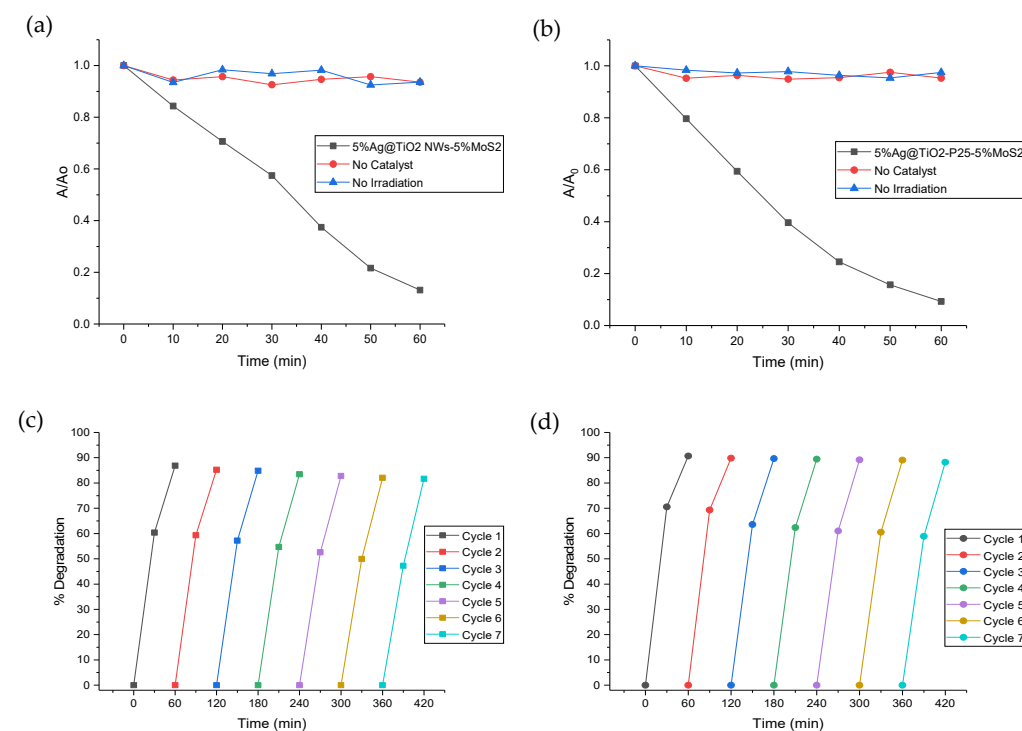

Figure 8. Control experiments and stability tests for 5%Ag@TiO$_2$NWs-5%MoS$_2$ (**a**,**c**), and 5%Ag@TiO$_2$-P25-5%MoS$_2$ (**b**,**d**) catalysts.

As shown in Figure 8, in all cases the last 10 min of the reaction produced only less than 10% degradation. This lack of degradation of the parent compound is due to the production of organic by-products during the photocatalytic process. This is confirmed by the stability studies in which it was demonstrated that after several cycles the photocatalyst is still viable for use since in any case less than 7% of efficiency is lost (see Figure 8c,d). Furthermore, it was demonstrated that, after 420 min of the reaction, the catalyst is able to degrade persistent organic pollutants by 80%. Furthermore, at any given cycle, catalysts can degrade more than 50% of the initial parent compound within the first 30 min of the reaction, demonstrating the stability and recyclability of the photocatalysts [44]. Table 4 shows the percentages of degradation and difference of the 5%Ag@TiO_2NWs-5%MoS_2 and 5%Ag@TiO_2-P25-5%MoS_2 catalysts after seven reaction cycles.

Table 4. Degradation and difference percentages of the 5%Ag@TiO_2NWs-5%MoS_2 and 5%Ag@TiO_2-P25-5%MoS_2 catalysts after seven cycles.

Catalyst.	Cycle	Degradation (%)	Difference (%)
5%Ag@TiO_2 NWs-5%MoS_2	1	86.87	6.34
	7	81.69	
5%Ag@TiO_2-P25-5%MoS_2	1	90.72	2.83
	7	88.22	

2.4. Hydrogen Production by Water Splitting

Figure 9 shows the hydrogen production by water splitting under irradiation at 320, 400, 500 and 600 nm. Table 5 shows the results corresponding to the highest hydrogen production from modified and unmodified silver-based catalysts. As can be seen, the catalysts with a MoS_2 loading of 20 wt.% produced the highest amount of hydrogen. Different studies [11–13] report that MoS_2 is a very active catalyst for hydrogen production, which, together with its low cost and abundance, makes it a relevant additive for different applications. Furthermore, experimental results together with density functional theory (DFT) simulations have shown that the catalytic activity of MoS_2 is due to unsaturated Mo-S sites along the edges [11–13] that can be designed for specific applications. When the H_2 production of the TiO_2 NWs catalysts is compared with those of TiO_2-P25, a significant difference is observed. This difference is mainly attributed to the difference of surface areas of the catalysts (see Table 1). In fact, previous works [16,22–25] have documented a direct relationship between hydrogen production and catalyst surface area. This behavior has been justified on the basis that higher surface areas provide charge separation in the form of trapping sites for photo-generated charge carriers [16,25].

At 320 nm (Figure 9a), the highest hydrogen production was obtained with the 5%Ag@TiO_2 NWs-20%MoS_2 catalyst (1480 μmol/hg). This amount represented a difference of 1424 μmol/hg, and was 26 times greater than the amount of hydrogen produced with the pristine TiO_2 NWs catalyst (56 μmol/hg). In the case of TiO_2-P25 catalysts, the highest hydrogen production was also obtained with the catalyst with a MoS_2 loading of 20 wt.% (5%Ag@TiO_2-P25-20%MoS_2; 1245 μmol/hg). This amount represented a difference of 1142 μmol/hg when compared to the pristine TiO_2-P25 (103 μmol/hg), and it was 12 times greater. Since no reduction in the hydrogen production was observed in any of the catalysts with increasing MoS_2 loadings, it is possible that higher amounts of hydrogen could be produced by incorporating loadings greater than 20 wt.%. Figure 9b shows the amount of hydrogen produced by the silver-based catalysts under irradiation at 400 nm. The catalysts with the highest hydrogen production were those with MoS_2 loadings of 20 wt.% (5%Ag@TiO_2 NWs-20%MoS_2, 5%Ag@TiO_2-P25-20%MoS_2) and highest surface areas. As was shown in the P25-based catalysts, the fact that no saturation in hydrogen production was observed indicates that an increase in MoS_2 loading could lead to even higher hydrogen productions than those observed. When irradiated with visible light (λ > 400 nm), the electrons of the AgNPs are excited due to the plasmon resonance and

injected into the CB of the TiO_2 [17], producing holes in the AgNPs that serve as oxidation agents that could lead to oxygen production or to their being quenched by a sacrificial electron donor [25]. The electrons that were injected to the conduction band of TiO_2 are gained by the water molecules, and hydrogen is produced. The maximum production of the 5%Ag@TiO_2 NWs-20%MoS_2 and 5%Ag@TiO_2-P25-20%MoS_2 catalysts was 1792 μmol/hg and 1344 μmol/hg, respectively, being ca. 32 % and 13 % greater than the amount obtained by the pristine TiO_2NWs (56 μmol/hg) and TiO_2-P25 catalysts (103 μmol/hg), respectively. At 500 nm (Figure 9c), 5%Ag@TiO_2 NWs-20%MoS_2 produced the maximum amount of hydrogen (1744 μmol/hg), which represents a difference of 1688 μmol/hg compared to the pristine TiO_2 NWs catalyst, being ca. 31 times higher. The amount of hydrogen produced by 5%Ag@TiO_2-P25-20%MoS_2 (1527 μmol/hg) was the maximum amount obtained by the TiO_2-P25 catalysts, and it was ca. 15 times greater than the pristine catalyst. As was observed under irradiation at other wavelengths, the hydrogen production depends on the surface area of the catalyst (the higher the surface area, the higher the hydrogen production), and the synergism created by the combination of the AgNPs and MoS_2. Figure 9d displays the amount of hydrogen produced by the silver-based catalysts with different MoS_2 loadings, under irradiation at 600 nm. The maximum amount of hydrogen was obtained again with the 20 wt.% MoS_2 loading, for both the TiO_2NWs (5%Ag@TiO_2 NWs-20%MoS_2; 1501 μmol/hg) and the TiO_2-P25 (5%Ag@TiO_2-P25-20%MoS_2; 1057 μmol/hg) catalysts. These amounts represented a difference of 1445 μmol/hg and 954 μmol/hg, respectively, when compared to the pristine TiO_2 catalysts, and were ca. 27 times and 10 times higher. The fact that the as-synthesized catalysts produce high amounts of hydrogen under low energy irradiation indicates a synergism among AgNPs, MoS_2 and the semiconductors, with a greater ability to use visible light.
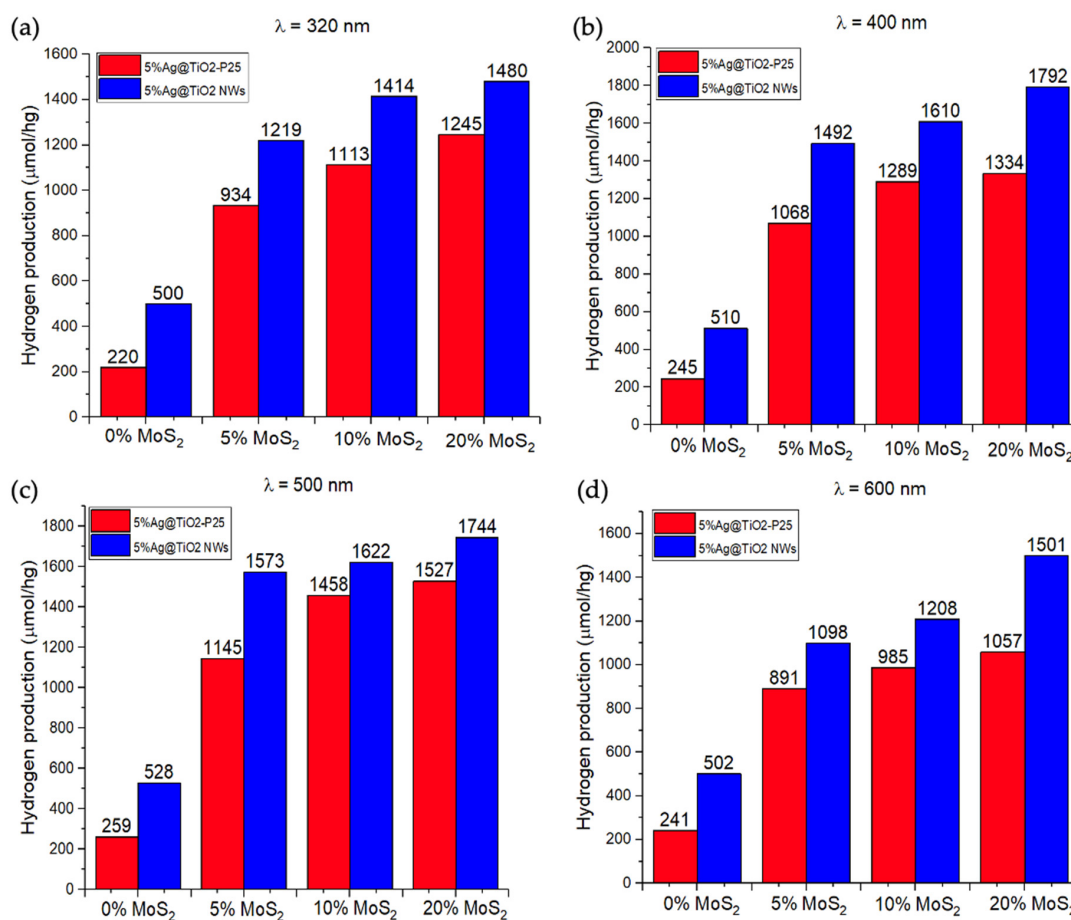

Figure 9. Hydrogen production of the TiO_2-based catalysts with different MoS_2 loadings under irradiation at 320 nm (**a**), 400 nm (**b**), 500 nm (**c**) and 600 nm (**d**).

Table 5. Maximum hydrogen production of the unmodified and modified TiO_2-based catalysts, under irradiation at different wavelengths.

Catalyst	Maximum H_2 Production (Unmodified Catalyst, µmol/hg) **	Maximum H_2 Production by the Modified Catalysts at Different Wavelengths (µmol/hg)			
		320 nm	400 nm	500 nm	600 nm
5%Ag@TiO_2NWs-20%MoS_2	56; TiO_2NWs	1480	1792	1744	1501
5%Ag@TiO_2-P25-20%MoS_2	103; TiO_2-P25	1245	1344	1527	1057

** Under irradiation at 320 nm.

The use of cut-off filters at different wavelengths made it possible to correlate the efficiency of the process with the ability to absorb radiation of different energy. As has been observed (Figure 9), the efficiency is maximized under irradiation at 400 nm, although the hydrogen production values at 500 nm are very similar, which indicates the extraordinary capacity of these catalysts for future applications using direct solar radiation. The results of recent studies on the production of hydrogen by water splitting using AgNPs and/or MoS_2 are shown in Table 6. As can be seen there, the amount of hydrogen reported by this study is one of the highest. However, a direct comparison with the other investigations cannot be made due to the fact that the experimental conditions, such as reaction time, crystal structures, reaction mixture, Ag and MoS_2 loadings, among others, are not the same.

Table 6. Recent research on photocatalytic hydrogen production using catalysts containing AgNPs or MoS_2.

Reference	H_2 Production (µmol/gh)	Source (nm)	Irradiation Time (h)	Crystal Structure of TiO_2 *	Reaction Mixture	Ag or MoS_2 (% wt.)
[45]	810	$\lambda > 400$	3	A:R	Water: Ethanol	1.5 (Ag)
[46]	23496	$\lambda = 254$	6	A:R	Water: $0.1N\ Na_2S + 0.1Na_2SO_3$	1.5 (Ag)
[25]	1119	$\lambda = 500$	2	R	Water : $0.5M\ Na_2S + 0.03M\ Na_2SO_3$	10 (Ag)
[47]	1600	$\lambda = 280–700$	4	A	Water: $0.35\ M\ Na_2S$ and $0.25\ M\ Na_2SO_3$	50 (MoS_2)
[48]	713.15	$\lambda = 250$	4	A/R	Water: TEOA	16 (MoS_2)
This work	1744	$\lambda = 400$	2	R	Water : $0.5M\ Na_2S$ and $0.03M\ Na_2SO_3$	5 (Ag) 20 (MoS_2)
This work	1527	$\lambda = 500$	2	A:R	Water : $0.5M\ Na_2S$ and $0.03M\ Na_2SO_3$	5 (Ag) 20 (MoS_2)

* A = Anatase, R = Rutile.

2.5. Mechanisms for the Degradation of Ciprofloxacin and the Production of Hydrogen

The possible mechanism of the photocatalytic degradation of ciprofloxacin by the Ag@TiO_2-MoS_2 catalysts is shown in Figure 10. Under ultraviolet light irradiation ($\lambda < 400$; Figure 10a), the electrons of the valence band of TiO_2 absorb the light and migrate to the conduction band of the semiconductor, leaving a hole in the valence band [49]. The hole created acts as oxidizing agent promoting the oxidation and degradation of ciprofloxacin [49]. The electrons that were promoted to the conduction band of the semiconductor could be gained by the AgNPs or the MoS_2, acting as electron buffers [49]. These electrons can interact with adsorbed oxygen molecules and create superoxide anions, which in turn can oxidize ciprofloxacin or react with water molecules to form hydroxyl radicals. These free radicals are very strong oxidizing agents; they can thus promote the degradation of the antibiotic. When irradiated with visible light ($\lambda > 400$, Figure 10b), the light does not have enough energy to promote an electron from the conduction band of TiO_2 due to its high band gap (3.20 eV for anatase, 3.0 eV for rutile); however, free electrons in AgNPs are stimulated by the plasmon resonance mechanism. These electrons can be injected in the conduction band of TiO_2 or into the surface of MoS_2 [50], giving rise to an interface between the Ag

NPs and the semiconductor, generating a Schottky barrier and a new Fermi level [51]. The electrons injected in the conduction band or into the surface of MoS_2 can react with adsorbed oxygen molecules, creating superoxide anions or hydroxyl radicals if they react with water molecules. Once the radicals are created, they can oxidize ciprofloxacin and thereby promote its degradation.
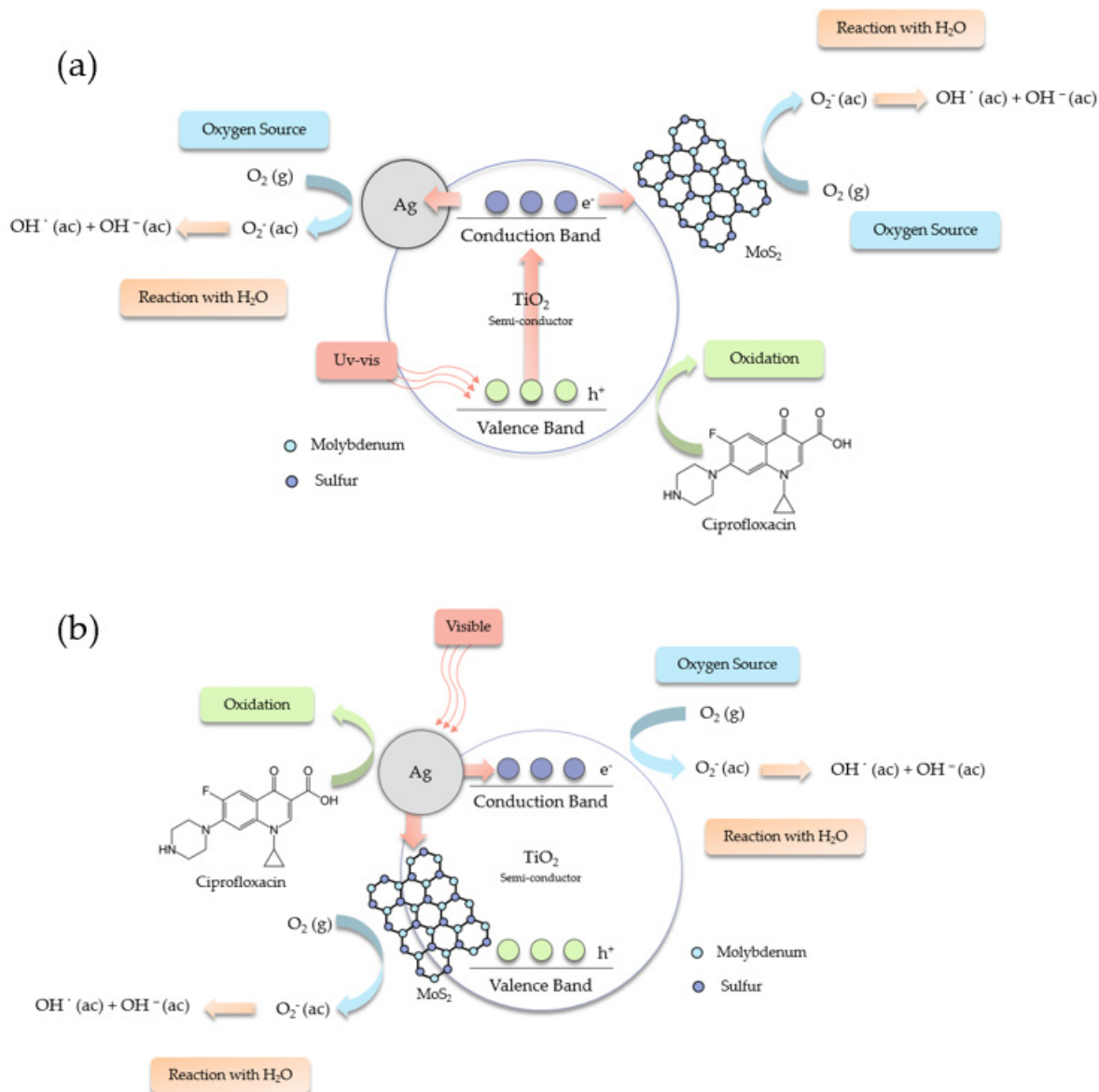

Figure 10. Proposed mechanism for the photodegradation of ciprofloxacin using $Ag@TiO_2$-MoS_2 catalysts under ultraviolet (**a**) and visible light (**b**).

Figure 11 shows the possible mechanism involved in the production of hydrogen by $Ag@TiO_2$-MoS_2 catalysts under ultraviolet and visible light. When irradiated with UV light (see Figure 11a), the electrons from the valence band of TiO_2 are photoexcited to the conduction band of the semiconductor [16,22]. As was described previously, these electrons can go to the MoS_2 or AgNPs. Once there, the electrons serve as catalytic sites for the production of hydrogen [25,50,51]. The holes that were created in the conduction band of the semiconductor act as oxidizing agents, producing oxygen. If sacrificing electron donors like SO_3^{2-}/SO_4^{2-} are used, then the holes will be quenched by them. This would decrease the possibility of recombination of the photoexcited electrons. When irradiated with visible light (Figure 11b), the AgNPs will produce the photoexcited electrons due to the surface

plasmon resonance effect. The electrons will be injected into the conduction band of the semiconductor and/or the surface of the MoS_2 [50,51]. These electrons have enough energy to reduce hydrogen ions and produce molecular hydrogen. The holes produced in the AgNPs, due to the injection of electrons to the conduction band of TiO_2 or into the surface of MoS_2, will be quenched by the sacrificing electron donors [50,51].
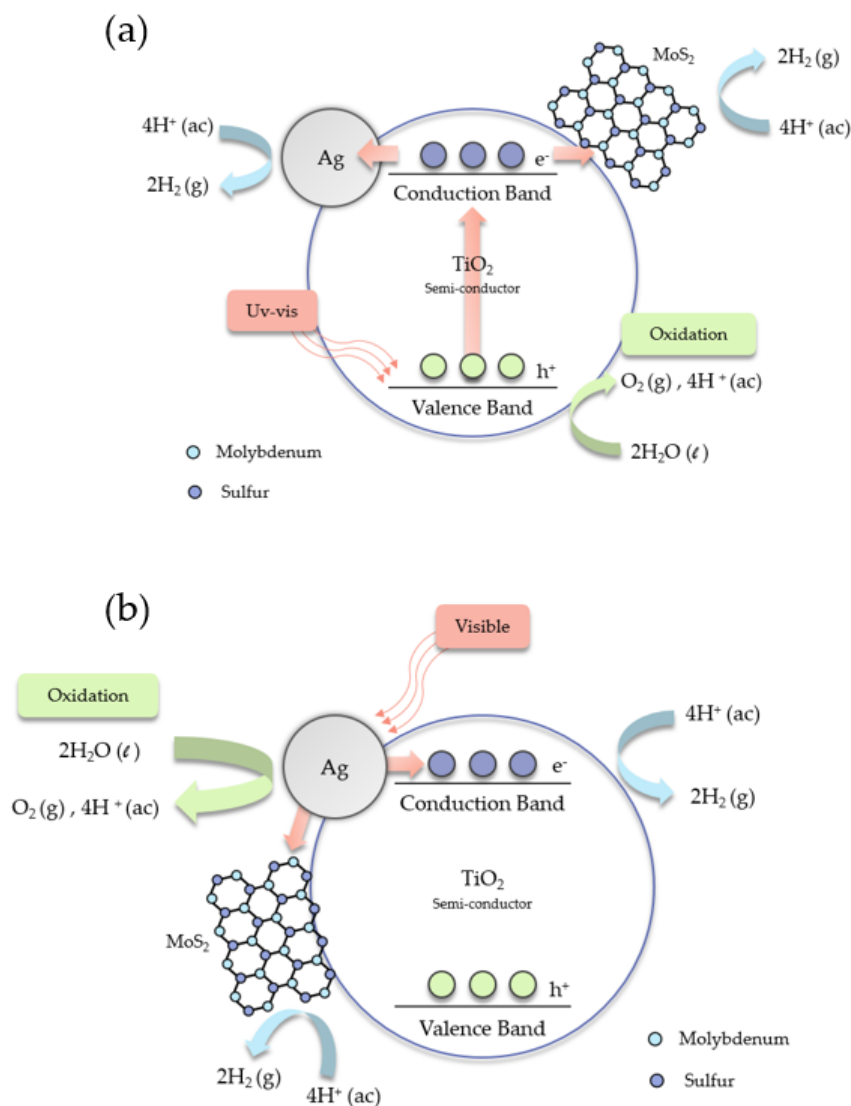

Figure 11. Mechanism proposed for the hydrogen production using Ag@TiO_2-MoS_2 catalysts under ultraviolet (**a**) and visible light (**b**).

3. Materials and Methods

3.1. Materials

All the reagents were used as received, without further purification. All the solutions were prepared using deionized water (Milli-Q water, 18.2 $M\Omega cm^{-1}$ at 25 °C). $TiCl_4$ (+99.9%), HCl 37% (ACS Reagent), Ethanol (95%), Acetone (HPLC plus, ≥99.9%), Ciprofloxacin ($C_{17}H_{18}FN_3O_3$, +98%) and Isopropyl alcohol (FCC, FG, +99.7%) were provided by Sigma Aldrich (Milwaukee, WI, USA). Silicon p-type boron-doped substrates (Si <100>), were provided by El-CAT (Ridgefield Park, NJ, USA). Sodium borohydride ($NaBH_4$, +99.9%), silver nitrate ($AgNO_3$, 99.99+%, trace metal basis), Na_2S (+99.9%), Na_2SO_3 (+98%) and MoS_2 (nanopowder, 90 nm diameter) were provided by Acros Chemical (Newark, NJ, USA). A total of 0.45 μm syringe filters were provided by Fisher Scientific (Pittsburgh, PA, USA).

3.2. Synthesis of Titanium Oxide Nanowires (TiO₂ NWs)

The synthesis of the titanium oxide nanowires (TiO$_2$ NWs) has been reported elsewhere [52]. In a typical synthesis, a 1:1 solution of water and HCl (37% solution) were mixed for ten minutes. After that, TiCl$_4$ (3 mL for each 100 mL solution) was added dropwise and left to mix for ten additional minutes. Then the solution was transferred to Teflon-lined autoclaves and silicon substrates, and Si<100> was incorporated into the solution. Once sealed, the autoclaves were transferred to an oven and heated at a temperature of 180 °C for 24 h. After that, the TiO$_2$ NWs grown on the Si substrates were separated from the support and thoroughly washed with deionized water. Subsequently, the material obtained was dried at 60 °C for two hours and stored in vials that were sealed until later use.

3.3. Incorporation of Ag NPs on TiO₂NWs and TiO₂-P25

The deposition of AgNPs on the surface of TiO$_2$ NWs and TiO$_2$-P25 is based on the method described by Naldoni and group [53]. In a typical synthesis, 500 mg of the support (TiO$_2$ NWs or TiO$_2$-P25) is dispersed in water and stirred for 30 min. After that, the desired amount of silver precursor (AgNO$_3$) is added to the solution and stirred for 10 additional minutes. Then a solution of sodium borohydride (10 mg in 10 mL of water) is added dropwise to the solution and left to react for 30 min. The product (5%Ag@TiO$_2$NWs or 5%Ag@TiO$_2$-P25) is centrifuged, washed with deionized water, and dried over night at 60 °C.

3.4. Incorporation of MoS₂ on 5%Ag@TiO₂ NWs and 5%Ag@TiO₂-P25

The incorporation of MoS$_2$ on the silver-based catalysts consisted in dispersing 500 mg of the desired catalyst (5%Ag@TiO$_2$NWs or 5%Ag@TiO$_2$-P25) in 100 mL of water, and subsequent stirring for 30 min. After that, different amounts of MoS$_2$ (5, 10, 20 wt.%) were added to the solution and stirred for 1 h. Then the final product was centrifuged, washed, collected and dried for 3 h at 60 °C. The catalysts were identified as 5%Ag@TiO$_2$NWs-5%MoS$_2$, 5%Au@TiO$_2$NWs-10%MoS$_2$, 5%Au@TiO$_2$NWs-20%MoS$_2$, 5%Au@TiO$_2$-P25-5%MoS$_2$, 5%Au@TiO$_2$-P25-10%MoS$_2$ and 5%Au@TiO$_2$-P25-20%MoS$_2$.

3.5. Characterization of the Catalysts

XPS measurements were carried out on an ESCALAB 220i-XL spectrometer, using the non-monochromated Mg Kα (1253.6 eV) radiation of a twin-anode, operating at 20 mA and 12 kV in the constant analyzer energy mode, with a PE of 40 eV. The crystalline phase of the catalysts was studied by X-ray diffraction (XRD), using a Bruker D8 Advance X-Ray diffractometer operating at 40 kV and 40 mA (Billerica, MA, USA) and Raman spectroscopy (DXR Thermo Raman Microscope, 532 nm laser source at 5 mW power with a resolution of 5 cm^{-1} (Waltham, MA, USA). The surface area of the composites was studied through the Brunauer–Emmett–Teller (BET) method using a Micromeritics ASAP 2020, according to N$_2$ adsorption isotherms at 77 K (Norcross, GA, USA). The morphology of the catalysts was studied by field-emission scanning electron microscopy coupled with energy-dispersive spectroscopy (FE-SEM; Philips XL30 S-FEG; Chatsworth, CA, USA) and high-resolution transmission electron microscopy (HRTEM, JEOL 3000F; Peabody, MA, USA).

3.6. Photocatalytic Experiments

To study the photodegradation of ciprofloxacin, a solution of 1×10^{-5} M of ciprofloxacin was prepared and mixed with the desired catalyst. After that, the pH was adjusted to 7 using a diluted solution of HCl or NaOH, and the solution was kept in the dark for 30 min under constant stirring. Then, 3 mL of a 0.005% H$_2$O$_2$ solution was added, and the reaction mixture was subjected to constant air bubbling to homogenize the solution and guarantee the presence of oxygen. The next step was to surround the solution with a solar simulator composed of two white light bulbs (60 watts), generating an illuminance of ca. 52000 lx. After the solar simulator was switched on, the reaction was monitored at 22 °C for 60 min, taking 5 mL aliquots every ten minutes. Before proceeding to the measurement of these

aliquots, the catalyst was removed from the solution using 0.45 μm membrane filters. The degradation of the antibiotic was studied using a Shimadzu UV-1800PC spectrophotometer.

The experimental setup to study the production of hydrogen via water splitting consisted in mixing 50 mg of the desired catalyst with 100 mL of deionized water in a 250 mL quartz reactor. Then, sacrificial electron donor solutions (Na_2SO_3, 0.02M; Na_2S, 0.4M) were added, and the reaction mixture was kept at 20 °C and purged with nitrogen (N_2) for 30 min. After that, the reaction mixture was irradiated using a solar simulator whose irradiation power in the absence of filters was 100 mWcm^{-2}. To demonstrate the influence of irradiation energy on the water splitting reaction, different cut-off filters at 320 nm, 400 nm, 500 nm and 600 nm were used and the reaction was followed for two hours. The hydrogen produced was collected and quantified using a gas chromatograph coupled with a thermal conductivity detector (GC–TCD, Perkin-Elmer Clarus 600).

4. Conclusions

Silver-TiO_2-based catalysts with different amounts of MoS_2 loadings (5, 10, 20 wt.%) were synthesized to study their photocatalytic activity by degrading the antibiotic ciprofloxacin in aqueous solution and the production of hydrogen via water splitting. All the modified catalysts were able to degrade more than 75% ciprofloxacin, with 5%Ag@TiO_2-P25-5%MoS_2 being the catalyst that obtained the highest degradation (ca. 91%). The TiO_2NW-based catalyst that showed the highest percentage of degradation was 5%Ag@TiO_2NWs-5%MoS_2, with an efficiency of ca. 87% in 60 min. The difference in degradation between TiO_2NWs and commercial TiO_2 (TiO_2-P25) is attributed to the morphology of the catalysts and their contact and interaction with the antibiotic. The route of degradation was proved to be photocatalysis, and the stability tests showed a loss of activity after seven cycles of ca. 3% and 6% for 5%Ag@TiO_2-P25-5%MoS_2 and 5%Ag@TiO_2 NWs-5%MoS_2, respectively. These results anticipate that these catalysts could have relevance for use in decontamination processes, especially of ciprofloxacin in aqueous solution. Currently, research with these catalysts is being extended to other fluoroquinolones whose impact on the environment is certainly worrying.

In terms of hydrogen production, the incorporation of AgNPs and MoS_2 allowed the catalysts to produce hydrogen under both ultraviolet and visible light. The 5%Ag@TiO_2 NWs-20%MoS_2 catalyst obtained the highest hydrogen production (1736 μmol/ hg), under irradiation at 400 nm. This amount was 32 times greater than the production of the pristine TiO_2 NWs (56 μmol/hg). For TiO_2-P25-based catalysts, the highest hydrogen production was produced by 5%Ag@TiO_2-P25-20%MoS_2 (1527 μmol/hg) under irradiation at 500 nm, being ca. 15 times greater than the amount obtained by the pristine TiO_2-P25 (103 μmol/hg). The high catalytic activity in the production of hydrogen was attributed to the synergism among AgNPs, MoS_2 and the high surface area of the catalysts. Since no reduction in the hydrogen production was observed with the increase in MoS_2 loadings, it could be possible that at higher MoS_2 loadings, higher production of hydrogen could be obtained.

As previously shown, the most efficient catalysts in the ciprofloxacin photodegradation process are less efficient in the hydrogen production reaction by water splitting. This behavior indicates that the reaction mechanisms of the catalysts for both processes are clearly different, which can be conveniently explained in future studies in which scavengers are used for both reactions, and the intermediate compounds generated are analyzed.

The catalysts synthesized in the present investigation showed a relevant photocatalytic activity. These catalysts are easy to prepare, friendly to the environment and have a very low economic cost; they could therefore be the starting point for the development of increasingly efficient catalysts that can be widely used for these applications.

References

1. Tiwari, A.; Gautam, A.; Sk, S.; Gavali, D.S.; Thapa, R.; Pal, U. Controlled Loading of MoS_2 on Hierarchical Porous TiO_2 for Enhanced Photocatalytic Hydrogen Evolution. *J. Phys. Chem. C* **2021**, *125*, 11950–11962. [CrossRef]
2. Jin, H.; Song, T.; Paik, U.; Qiao, S.-Z. Metastable Two-Dimensional Materials for Electrocatalytic Energy Conversions. *Acc. Mater. Res.* **2021**, *2*, 559–573. [CrossRef]
3. Borthakur, P.; Boruah, P.K.; Das, M.R.; Ibrahim, M.M.; Altalhi, T.; El-Sheshtawy, H.S.; Szunerits, S.; Boukherroub, R.; Amin, M.A. CoS_2 Nanoparticles Supported on RGO, g-C_3N_4, BCN, MoS_2, and WS_2 Two-Dimensional Nanosheets with Excellent Electrocatalytic Performance for Overall Water Splitting: Electrochemical Studies and DFT Calculations. *ACS Appl. Energy Mater.* **2021**, *4*, 1269–1285. [CrossRef]
4. Chen, X.; Liu, Y.; Gao, W.; Yang, G.; Qureshi, A.H.; Chen, M.; Yao, X.; Zhou, M.; Zhang, X.; Liu, Y. High Electrocatalytic Activity of Defected MX_2/Graphene Heterostructures (M = Mo, W.; X = S, Se) for Hydrogen Evolution Reaction. *J. Phys. Chem. C* **2021**, *125*, 15292–15300. [CrossRef]
5. Brinda, K.N.; Malecki, J.G.; Yhobu, Z.; Nagaraju, D.H.; Budagumpi, S.; Erakulan, E.S.; Thapa, R. Novel Carbene Anchored Molecular Catalysts for Hydrogen Evolution Reactions. *J. Phys. Chem. C* **2021**, *125*, 3793–3803. [CrossRef]
6. Pan, Y.; Chen, S. Influence of Group Iii and Iv Elements on the Hydrogen Evolution Reaction of MoS_2 Disulfide. *J. Phys. Chem. C* **2021**, *125*, 11848–11856.
7. Rusinque, B.; Escobedo, S.; de Lasa, H. Hydrogen Production via Pd-TiO_2 Photocatalytic Water Reaction Mechanism. *Catalysts* **2021**, *11*, 405. [CrossRef]
8. Tahir, M. Investigating the Influential Effect of Etchant Time in Constructing 2D/2D HCN/MXene Heterojunction with Controlled Growth of TiO_2NPs for Stimulating Pho.otocatalytic H_2Production. *Energy Fuels* **2021**, *35*, 6807–6822. [CrossRef]
9. Wang, S.; Zhang, J.; Li, B.; Sun, H.; Wang, S. Engineered Graphitic Carbon Nitride-Based Photocatalysts for Visible-Light-Driven Water Splitting: A Review. *Energy Fuels* **2021**, *35*, 6504–6526. [CrossRef]
10. Kwon, H.; Bae, D.; Won, D.; Kim, H.; Kim, G.; Cho, J.; Park, H.J.; Baik, H.; Jeong, A.R.; Lin, C.H.; et al. Nanoporous Silver Telluride for Active Hydrogen Evolution. *ACS Nano* **2021**, *15*, 6540–6550. [CrossRef]
11. Li, Y.; Zuo, S.; Li, Q.H.; Wu, X.; Zhang, J.; Zhang, H.; Zhang, J. Vertically Aligned MoS_2 with In-Plane Selectively Cleaved Mo−S Bond for Hydrogen Production. *Nano Lett.* **2021**, *21*, 1848–1855. [CrossRef] [PubMed]
12. Qin, J.; Xi, C.; Zhang, R.; Liu, T.; Zou, P.; Wu, D.; Guo, Q.; Mao, J.; Xin, H.; Yang, J. Activating Edge-Mo of 2H-MoS_2 via Coordination with Pyridinic N-C for PH-Universal Hydrogen Evolution Electrocatalysis. *ACS Catal.* **2021**, *11*, 4486–4497. [CrossRef]
13. Singh, V.K.; Gupta, U.; Mukherjee, B.; Chattopadhyay, S.; Das, S. MoS_2 Nanosheets on $MoNi_4$/MoO_2Nanorods for Hydrogen Evolution. *ACS Appl. Nano Mater.* **2021**, *4*, 886–896. [CrossRef]
14. Chen, L.; Yang, Z.; Chen, B. Uniformly Dispersed Metal Sulfide Nanodots on G-C_3N_4 as Bifunctional Catalysts for High-Efficiency Photocatalytic H_2 and H_2O_2 Production under Visible-Light Irradiation. *Energy Fuels* **2021**, *35*, 10746–10755. [CrossRef]
15. Xu, Q.; Zhang, Y.; Zheng, Y.; Liu, Y.; Tian, Z.; Shi, Y.; Wang, Z.; Ma, J.; Zheng, W. Synergistic Effects of Tungsten Doping and Sulfur Vacancies in MoS_2 on Enhancement of Hydrogen Evolution. *J. Phys. Chem. C* **2021**, *125*, 11369–11379. [CrossRef]
16. Pinilla, S.; Machín, A.; Park, S.H.; Arango, J.C.; Nicolosi, V.; Márquez-Linares, F.; Morant, C. TiO_2-Based Nanomaterials for the Production of Hydrogen and the Development of Lithium-Ion Batteries. *J. Phys. Chem. B* **2018**, *122*, 972–983. [CrossRef]

17. Platero, F.; López-Martín, A.; Caballero, A.; Rojas, T.C.; Nolan, M.; Colón, G. Overcoming Pd-TiO$_2$ Deactivation during H$_2$ Production from Photoreforming Using Cu@Pd Nanoparticles Supported on TiO$_2$. *ACS Appl. Nano Mater.* **2021**, *4*, 3204–3219. [CrossRef]

18. Li, Z.; Jiang, Z.; Zhou, W.; Chen, M.; Su, M.; Luo, X.; Yu, T.; Yuan, C. MoS2Nanoribbons with a Prolonged Photoresponse Lifetime for Enhanced Visible Light Photoelectrocatalytic Hydrogen Evolution. *Inorg. Chem.* **2021**, *60*, 1991–1997. [CrossRef]

19. Özgür, D.Ö.; Özkan, G.; Atakol, O.; Çelikkan, H. Facile Ion-Exchange Method for Zn Intercalated MoS$_2$ As an Efficient and Stable Catalyst toward Hydrogen Evaluation Reaction. *ACS Appl. Energy Mater.* **2021**, *4*, 2398–2407. [CrossRef]

20. Lin, H.; Ma, X.; Wang, H.; Wang, B.; Li, S.X.; Yi, X.; Li, Y.Y.; Wang, L. Promoted Interfacial Charge Transport and Separation of Size-Uniform Zn, Ni-Doped CdS-1T/2H O-MoS$_2$ Nanoassemblies for Efficient Visible-Light Photocatalytic Water Splitting. *Cryst. Growth Des.* **2021**, *21*, 1278–1289. [CrossRef]

21. Huerta-Aguilar, C.A.; García-Gutiérrez, Y.S.; Thangarasu, P. Crystal plane directed interaction of TiO$_2$ [1 0 1] with AgNPs [1 1 1] silver nanoparticles enhancing solar light induced photo-catalytic oxidation of ciprofloxacin: Experimental and theoretical studies. *Chem. Engi. J.* **2020**, *394*, 124286. [CrossRef]

22. Machín, A.; Cotto, M.; Ducongé, J.; Arango, J.C.; Morant, C.; Márquez, F. Synthesis and Characterization of Au@TiO$_2$ NWs and their Catalytic Activity by Water Splitting: A Comparative Study with Degussa P25. *AJEAS* **2017**, *10*, 298–311.

23. Machín, A.; Cotto, M.; Duconge, J.; Arango, J.C.; Morant, C.; Pinilla, S.; Soto-Vázquez, L.; Resto, E.; Márquez, F. Hydrogen production via water splitting using different Au@ZnO catalysts under UV–vis irradiation. *J. Photochem. Photobiol. A Chem.* **2018**, *353*, 385–394. [CrossRef]

24. Machín, A.; Arango, J.C.; Fontánez, K.; Cotto, M.; Duconge, J.; Soto-Vázquez, L.; Resto, E.; Petrescu, F.I.T.; Morant, C.; Márquez, F. Biomimetic Catalysts Based on Au@ZnO–Graphene Composites for the Generation of Hydrogen by Water Splitting. *Biomimetics* **2020**, *5*, 39. [CrossRef] [PubMed]

25. Machín, A.; Soto-Vázquez, L.; Colón-Cruz, C.; Valentín-Cruz, C.A.; Claudio-Serrano, G.J.; Fontánez, K.; Resto, E.; Petrescu, F.I.; Morant, C.; Márquez, F. Photocatalytic Activity of Silver-Based Biomimetics Composites. *Biomimetics* **2021**, *6*, 4. [CrossRef] [PubMed]

26. Liu, J.; Liu, Z.; Piao, C.; Li, S.; Tang, J.; Fang, D. Construction of Fixed Z-Scheme Ag AgBr/Ag/TiO$_2$ Photocatalyst Composite Film for Malachite Green Degradation with Simultaneous Hydrogen Production. *J. Power Sources* **2020**, *469*, 228430. [CrossRef]

27. Lu, L.; Wang, G.; Xiong, Z.; Hu, Z.; Liao, Y.; Wang, J.; Li, J. Enhanced Photocatalytic Activity under Visible Light by the Synergistic Effects of Plasmonics and Ti^{3+} Doping at the Ag/TiO$_{2-x}$ Heterojunction. *Ceram. Int* **2020**, *46*, 1–11. [CrossRef]

28. Soto-Vázquez, L.; Rolón-Delgado, F.; Rivera, K.; Cotto, M.C.; Duconge, J.; Morant, C.; Pinilla, S.; Márquez-Linares, F. Catalytic use of TiO$_2$ nanowires in the photodegradation of Benzophenone-4 as an active ingredient in sunscreens. *J. Environ. Manag.* **2019**, *247*, 822–828. [CrossRef]

29. Bharti, B.; Kumar, S.; Lee, H.; Kumar, R. Formation of Oxygen Vacancies and Ti^{3+} State in TiO$_2$ Thin Film and Enhanced Optical Properties by Air Plasma Treatment. *Sci. Rep.* **2016**, *6*, 1–12. [CrossRef]

30. Ho, Y.; Ma, C.; Luong, T.; Wei, L.; Yen, T.; Hsu, W.; Chang, W.; Chu, Y.; Tu, Y.; Pande, K.P.; et al. Layered MoS$_2$ Grown on c -Sapphire by Pulsed Laser Deposition. *Phys. Status Solidi Rapid Res. Lett.* **2015**, *191*, 187–191. [CrossRef]

31. Zhang, C.; Wang, Z.; Bhoyate, B.; Morey, T.; Neria, B.L.; Vasiraju, V.; Gupta, G.; Palchoudhury, S.; Kahol, P.K.; Mishra, S.R.; et al. MoS$_2$ Decorated Carbon Nanofibers as Efficient and Durable Electrocatalyst for Hydrogen Evolution Reaction. *J. Carbon Res.* **2017**, *3*, 33. [CrossRef]

32. Uddin, M.J.; Cesano, F.; Chowdhury, A.R.; Trad, T.; Cravanzola, S.; Martra, G.; Lorenzo, M.; Zecchina, A.; Scarano, D. Surface Structure and Phase Composition of TiO$_2$ P25 Particles After Thermal Treatments and HF. *Etching Front. Mater.* **2020**, *7*, 192. [CrossRef]

33. Ibukun, O.; Evans, P.E.; Dowben, P.A.; Jeong, H.K. Titanium dioxide-molybdenum disulfide for photocatalytic degradation of methylene blue. *Chem. Phys.* **2019**, *1*, 110419. [CrossRef]

34. Askari, M.B.; Kalourazi, A.F.; Seifi, M.; Shahangian, S.S.; Askari, N.; Manjili, T.J. Hydrothermal Synthesis of Molybdenum Disulfide (MoS2) and Study of Structure, Optical, Electrical and High Antibacterial Properties. *Optik* **2018**, *174*, 154–162. [CrossRef]

35. Li, M.; Cui, Z.; Li, E. Silver-Modified MoS$_2$ Nanosheets as a High-Efficiency Visible-Light Photocatalyst for Water Splitting. *Ceram. Int.* **2019**, *45*, 14449–14456. [CrossRef]

36. Han, E.; Vijayarangamuthu, K.; Youn, J.; Park, Y.K.; Jung, S.C.; Jeon, K.J. Degussa P25 TiO$_2$ modified with H$_2$O$_2$ under microwave treatment to enhance photocatalytic properties. *Catal. Today* **2018**, *303*, 305–312. [CrossRef]

37. Suriani, A.B.; Muqoyyanah; Mohamed, A.; Othman, M.H.D.; Mamat, M.H.; Ahmad, M.K.; Nayan, N.; Khalil Abdul, H.P.S. Reduced graphene oxide-multiwalled carbon nanotubes hybrid film with low Pt loading as counter electrode for improved photovoltaic performance of dye-sensitized solar cells. *J. Mater. Sci. Mater. Electron.* **2018**, *1*, 10723–10743. [CrossRef]

38. Stamplecoskie, K.G.; Scaiano, J.C. Optimal Size of Silver Nanoparticles for Surface-Enhanced Raman Spectroscopy. *J. Phys. Chem.* **2011**, *115*, 1403–1409. [CrossRef]

39. Lu, Y.; Feng, S.; Liu, X.; Chen, L. Surface-enhanced Raman Scattering Study of Silver Nanoparticles Prepared by Using MC as a Template. *J. Nanomat.* **2013**, *1*, 984831. [CrossRef]

40. Wang, C.; Zhan, Y.; Wang, Z. TiO$_2$, MoS$_2$, And Tio$_2$/MoS$_2$ Heterostructures for Use in Organic Dyes Degradation. *Chem. Select.* **2018**, *3*, 1713–1718. [CrossRef]

41. Malakootian, M.; Nasiri, A.; Gharaghani, M.A. Photocatalytic Degradation of Ciprofloxacin Antibiotic by TiO$_2$ Nanoparticles Immobilized on a Glass Plate. *Chem. Eng. Comm.* **2019**, *207*, 56–72. [CrossRef]

42. Costa, L.N.; Nobre, F.X.; de Oliveira Lobo, A.; de Matos, J.M.E. Photodegradation of Ciprofloxacin Using TiO$_2$/SnO$_2$ Nanostructures. *Environ. Nanotech. Monit. Manag.* **2021**, *16*, 100466.

43. He, J.; Du, Y.; Bai, Y.; An, J.; Cai, X.; Chen, Y.; Wang, P.; Yang, X.; Feng, O. Facile Formation of Anatase/Rutile TiO$_2$ Nanocomposites with Enhanced Photocatalytic Activity. *Molecules* **2019**, *24*, 2996. [CrossRef]

44. Khan, S.A.; Arshad, Z.; Shahid, S.; Arshad, I.; Rizwan, K.; Sher, M.; Fatima, U. Synthesis of TiO$_2$/Graphene Oxide Nanocomposites for Their Enhanced Photocatalytic activity Against Methylene Blue Dye and Ciprofloxacin. *J. Com. B.* **2019**, *175*, 107120. [CrossRef]

45. Liu, E.; Kang, L.; Yang, Y.; Sun, T.; Hu, X.; Zhu, C.; Liu, H.; Wang, Q.; Li, X.; Fan, J. Plasmonic Ag Deposited TiO$_2$ Nano-Sheet Film for Enhanced Photocatalytic Hydrogen Production by Water Splitting. *Nanotechnology* **2014**, *25*, 165401. [CrossRef]

46. Gogoi, D.; Namdeo, A.; Golder, A.K.; Peela, N.R. Ag-Doped TiO$_2$ Photocatalysts with Effective Charge Transfer for Highly Efficient Hydrogen Production through Water Splitting. *Int. J. Hydrogen. Energy* **2020**, *45*, 2729–2744. [CrossRef]

47. Zhou, W.; Yin, Z.; Du, Y.; Huang, X.; Zeng, Z.; Fan, Z.; Liu, H.; Wang, J.; Zhang, H. Synthesis of Few-Layer MoS$_2$ Nanosheet-Coated TiO$_2$ Nanobelt Heterostructures for Enhanced Photocatalytic Activities. *Small* **2013**, *9*, 140–147. [CrossRef]

48. Ou, W.; Pan, J.; Liu, Y.; Li, S.; Li, H.; Zhao, W.; Wang, J.; Song, C.; Zheng, Y.; Li, C. Two-Dimensional Ultrathin MoS$_2$-Modified Black Ti3$^+$–TiO$_2$ Nanotubes for Enhanced Photocatalytic Water Splitting Hydrogen Production. *J. Energy Chem.* **2020**, *43*, 188–194. [CrossRef]

49. Lima, A.S.; Rocha, R.D.C.; Pereira, E.C. Photodegradation of Ciprofloxacin antibiotic over TiO$_2$ grown by PEO: Ecotoxity response in *Lactuca sativa* L. and *Lemna minor*. *Int. J. Environ. Sci. Technol* **2021**, 1–10. [CrossRef]

50. Saravanan, R.; Manoj, D.; Qin, J.; Naushad, M.; Gracia, F.; Lee, A.F.; Khan, M.M.; Gracia-Pinilla, M.A. Mechanothermal synthesis of Ag/TiO$_2$ for photocatalytic methyl orange degradation and hydrogen production. *Process Saf. Environ. Prot.* **2018**, *120*, 339–347. [CrossRef]

51. Lin, Y.; Renb, P.; Wei, C. Fabrication of MoS$_2$/TiO$_2$ heterostructures with enhanced photocatalytic activity. *CrystEngComm* **2019**, *21*, 3439–3450. [CrossRef]

52. Cotto, M.T.; Campo, E.; Gómez, A.; Morant, C.; Márquez, F. Photocatalytic degradation of rhodamine-B under UV-visible light irradiation using different nanostructured catalysts. *Am. Chem. Sci. J.* **2013**, *3*, 178–202. [CrossRef]

53. Naldoni, A.; D'Arienzo, M.; Altomare, M.; Marelli, M.; Scotti, R.; Morazzoni, F.; Selli, E.; Dal Santo, V. Pt and Au/TiO$_2$ photocatalysts for methanol reforming: Role of metal nanoparticles in tuning charge trapping properties and photoefficiency. *Appl. Catal. B* **2013**, *130*, 239–248. [CrossRef]